³Centre for

The concept of dual-boundary forcing in land surface-subsurface interactions of the terrestrial hydrologic and energy cycles

M. Rahman¹, M. Sulis¹, S. Kollet^{2,3}

¹Meteorological Institute, University of Bonn, Germany

²Institute for Bio- and Geosciences, Agrosphere, Research Centre Juelich, Germany

³Centre for High-Performance Scientific Computing in Terrestrial System, HPSC TerrSys

This article has been accepted for publication and undergone full peer review but has not been through the copyediting, typesetting, pagination and proofreading process which may lead to differences between this version and the Version of Record. Please cite this article as an 'Accepted Article', doi: 10.1002/2014WR015738

Abstract

Terrestrial hydrological processes interact in a complex, non-linear fashion. It is important to quantify these interactions to understand the overall mechanisms of the coupled water and energy cycles. In this study, the concept of a dual boundary forcing is proposed that connects the variability of atmospheric (upper boundary) and subsurface (lower boundary) processes to the land surface mass and energy balance components. According to this concept, the spacetime patterns of land surface mass and energy fluxes can be explained by the variability of the dominating boundary condition for the exchange processes, which is determined by moisture and energy availability. A coupled subsurface-land surface model is applied on the Rur catchment, Germany, to substantiate the proposed concept. Spectral and geostatistical analysis on the observations and model results show the coherence of different processes at various space-time scales in the hydrological cycle. The spectral analysis shows that atmospheric radiative forcing generally drives the variability of the land surface energy fluxes at the daily time scale, while influence of subsurface hydrodynamics is significant at monthly to multimonth time scales under moisture limited conditions. The geostatistical analysis demonstrates that atmospheric forcing and groundwater control the spatial variability of land surface processes under energy and moisture limited conditions, respectively. These results suggest that under moisture limited conditions, groundwater influences the variability of the land surface mass and energy fluxes. Under energy limited conditions, on the contrary, variability of land surface processes can be explained by atmospheric forcing alone.

1. Introduction

Atmospheric and subsurface processes show variability at different space-time scales [e.g., *Kumar and Georgiou*, 1993; *Haddad et al.*, 2004; *Gundogdu and Guney*, 2007; *Táany et al.*, 2009; *Beecham and Chowdhury*, 2010]. Land surface connects these two compartments (i.e., atmosphere and subsurface) of the hydrological cycle. Because of the direct interactions, land surface processes (e.g., evapotranspiration, ET and sensible heat transfer) are influenced by the variability of atmosphere and subsurface hydrodynamics.

The connection between subsurface hydrodynamics and land surface mass and energy fluxes has been a subject of research for some time [e.g., Tian et al., 2012; Niu et al., 2013]. Sklash and Farvolden [1979] discussed the important role of groundwater on surface runoff generation using observations and simulation results. Liang et al. [2003] showed the impact of the surface water-groundwater interactions on land surface processes. Maxwell and Miller [2005] demonstrated the effect of including detailed subsurface hydrodynamics in a land surface parameterization scheme for simulating the coupled water and energy cycles. Kollet and Maxwell [2008] studied the influence of groundwater dynamics on land surface energy fluxes and proposed a critical water table depth (WTD) zone where the effect is significant along hillslopes. Similar relationship between ET and WTD was found by Szilagyi et al. [2013], who used observations from Platte river valley, USA. Observations [Yeh and Eltahir, 2005] and model results [e.g., Miguez-Macho and Fan, 2012a] also reveal the role of groundwater as a modulator of surface runoff. The groundwater control on ET through shallow soil moisture has been investigated explicitly in several studies [e.g., Chen and Hu, 2004; Soylu et al., 2011]. Lam et al. [2011] studied the spatial and temporal connection between groundwater dynamics and ET and showed the importance of groundwater contribution towards dry season evaporation. The study by Miguez-Macho and Fan [2012b] demonstrated the influence of groundwater on ET at a seasonal scale and discussed different

mechanisms responsible for this phenomenon. Several studies have demonstrated the scaling properties of groundwater dynamics and showed the connection with surface water system [e.g., *Little and Bloomfield*, 2010; *Schilling and Zhang*, 2012] and energy fluxes [e.g., *Amenu et al.*, 2005].

The interaction between land surface processes and atmospheric variables has also been studied previously [e.g., *Brubaker and Entekhabi*, 1996; *Betts et al.*, 1996; *Porporato et al.*, 2000]. Several studies demonstrated the effect of land surface soil moisture [e.g., *Manabe and Delworth*, 1990; *Rowell and Blondin*, 1990; *Findell and Eltahir*, 1997; *Seuffert et al.*, 2002; *Gedney and Cox*, 2003; *Zhang et al.*, 2008] and groundwater dynamics [e.g., *Maxwell et al.*, 2007; *Yuan et al.*, 2008] on atmospheric processes. The important role of groundwater dynamics on land-atmosphere moisture feedback was discussed by *York et al.* [2002]. *Anyah et al.* [2008] showed the effect of subsurface hydrodynamics on coupled land-atmosphere variability and argued that a shallow groundwater table tends to enhance *ET* in arid regions, which eventually leads to increased precipitation. *Ferguson and Wood* [2011] used global satellite remote sensing data to identify the regions where land-atmosphere coupling persists. *Phillips and Klein* [2014] used the observations from Southern Great Plains, USA, and showed the influence of atmospheric forcing on land surface processes at daily time scale.

The aforementioned studies suggest that interconnections exist between different compartments of the terrestrial hydrological cycle (i.e., subsurface, land surface, and atmosphere). However, quantifying these interconnections between the compartmental mass and energy fluxes is complicated. This is mainly due to the diverse space-time scales associated with the processes that comprise this system, which has been discussed previously in relation to the variability in atmospheric [e.g., *Matsoukas et al.*, 2000; *Hsu and Li*, 2010], land surface [e.g., *Smith et al.*, 1998; *Labat et al.*, 2005; *Ding et al.*, 2013] and subsurface

[e.g., *Liang and Zhang*, 2013] processes, as well as land-atmosphere interactions [e.g., *Delworth and Manabe*, 1993; *Wu and Dickinson*, 2004].

In this context, we propose the concept of a dual-boundary forcing (DBF) to represent and quantify the interactions between the compartmental mass and energy balance components at the relevant space and time scales. Arguably, it is not feasible to fully characterize these interactions with observations. Continuous measurements of all the fluxes and states from each compartment of the hydrological cycle covering the entire catchment for extended time periods would be required for this purpose, which are generally not available [e.g., Seneviratne and Stöckli, 2008; Fernández-Prieto et al., 2013]. Therefore, to support the proposed concept, we apply the coupled subsurface-land surface model ParFlow.CLM [Maxwell and Miller, 2005; Kollet and Maxwell, 2008] to a regional scale catchment (on the order of 10³km²) in Germany to simulate the spatially distributed mass and energy fluxes in the hydrological cycle over three consecutive years (2009-2011). The coupled model consists of the groundwater/surface water flow model ParFlow [Ashby and Falgout, 1996; Jones and Woodward, 2001; Kollet and Maxwell, 2006] and the Common Land Model (CLM, [Dai et al., 2003]). In the first step, we demonstrate the model's capability to represent the magnitude and dynamics of different processes in the hydrological cycle by comparing the model results with spatially-distributed measurements. In ensuing steps, we analyze measured and simulated mass and energy fluxes using spectral and geostatistical analysis techniques. The results illustrate scale-dependent coherence between groundwater dynamics and land surface processes, which substantiate the proposed DBF concept.

2. Conceptual approach

The underlying hypothesis of this study is that the land surface processes are influenced by a DBF at different space-time scales. According to this hypothesis, the atmosphere and

groundwater act as the upper and the lower boundaries, respectively. The availability of energy and moisture determines which boundary condition dominates the exchange processes. The land surface reacts and interacts at the interface between the free atmosphere and subsurface to adapt or transform the variability of the processes associated with those boundaries. Therefore, the space-time patterns in land surface processes can be in large parts explained by the variability of the dominant boundary condition at the respective space and time scales, when accounting for major non-linear feedbacks.

Figure 1 shows a schematic of the proposed DBF concept. Hypothetical time series of atmospheric and land surface (net radiation, R_{net} ; latent heat flux, LE; and potential latent heat flux, LE_{pot}), and subsurface (groundwater table depth, WTD) fluxes and states are shown in this figure. Coherence between atmospheric and land surface processes is observed under both energy limited and moisture limited conditions. Under energy limited conditions, LE agrees well with LE_{pot} because moisture is abundant. Under moisture limited conditions, the groundwater contribution becomes essential to meet the daily ET demand. Because of this dependence, the high frequency (daily) variability of land surface energy fluxes is propagated into the subsurface, generating the variability in subsurface hydrodynamics at the respective time scale [e.g., Gribovszki et al., 2010; Fahle and Dietrich, 2014]. The subsurface hydrodynamics, in contrast, influence the low frequency variability of the land surface processes under soil moisture limited conditions resulting in the increasing difference between LE_{pot} and LE in Figure 1. The controlling effect of the low frequency variability of subsurface hydrodynamics on land surface energy fluxes has been discussed by Amenu et al. [2005], who also suggested that this influence may be significant under dry conditions.

The proposed concept may be corroborated via the analysis of *in-situ* observations and physics based simulations of moisture and energy states and fluxes. It should be mentioned that the DBF concept may be simplified compared to the actual non-linear feedbacks between

the mass and energy balance components in the hydrological cycles. In this study, we applied a physics based distributed model, which incorporates mathematical formulations to represent complex processes of the coupled terrestrial hydrological and energy cycles to the best of our current knowledge. There is uncertainty with respect to model parameterization and structure, input parameters, and space/time discretization of the governing partial differential equations [e.g., *Vrugt et al.*, 2005]. Accounting for all sources of uncertainty is not feasible in the current modeling framework, because of the limitations of computational resources. However, the capability of the model to reproduce the major states and fluxes is tested by comparing the results with measured data from the experimental catchment. Additionally, there may be significant feedbacks from the land surface processes and subsurface hydrodynamics to the free atmosphere, which may also affect the connections between the mass and energy balance components at different space-time scales. We do not consider these here, because the model is forced with the atmospheric variables in offline mode.

3. Methods

3.1 The study area: Rur catchment

The study area is the Rur catchment (Figure 2a), which is located in western Germany with an area of about 2,400km². The Rur River has a length of some 165km with headwaters located in Belgium and discharge into the Meuse River near Maastricht. The northern part of the catchment is characterized by flat lowland regions, which is a part of the Belgium-Germany loess belt formed by unconsolidated rock deposits. Agriculture is the major land use type in this part of the catchment. This flat region receives an annual precipitation of approximately 600-800mm and contributes to a potential *ET* of approximately 550-600mm/a [*Bogena et al.*, 2005].

The southern part of the catchment is characterized by the mountainous Eifel region, where Palaeozoic and Mesozoic rock outcrops. Compared to the northern lowlands, this mountainous region is characterized by a higher precipitation amount of more than 1200mm/a and a lower potential *ET* amount of approximately 550mm/a [*Bogena et al.*, 2005]. The Eifel is heavily forested with coniferous trees. A distinct difference in the mean annual temperature between the northern (8.5-10.5°C) and the southern (7.0-9.0°C) part of the catchment is observed due a 600m difference in elevation.

3.2 The coupled model: ParFlow.CLM

ParFlow is an integrated, parallel, variably saturated groundwater flow model that solves the Richards' equation [*Richards*, 1931] in three spatial dimensions:

$$S_{s}\theta \frac{\partial \psi}{\partial t} + \phi \frac{\partial \theta(\psi)}{\partial t} = \nabla \cdot \mathbf{q} + S \tag{1}$$

$$\mathbf{q} = -k(x)k_r(\psi)\nabla(\psi - z) \tag{2}$$

where S_s is specific storage [m⁻¹], θ is soil moisture [-], ψ is pressure head [m], t is time [s], ϕ is porosity [-], \mathbf{q} is water flux [ms⁻¹], S is general source/sink term [s⁻¹], k(x) is saturated hydraulic conductivity [ms⁻¹], k(r) is relative permeability [-], and z is depth below surface [m]. ParFlow uses a cell-centered finite-difference/finite control volume scheme in space and an implicit backward Euler scheme in time to solve this equation. The surface flow is integrated by applying a free surface overland flow boundary condition at the land surface [Kollet and Maxwell, 2006]. The kinematic wave equation is solved maintaining the continuity of pressure and flux at the boundary. A terrain following vertical grid can be used in ParFlow honoring the topographic slopes in an approximate fashion [Maxwell, 2013].

The land surface model CLM is coupled with ParFlow to simulate land surface mass and energy balance components [Maxwell and Miller, 2005; Kollet and Maxwell, 2008]. Vertical

mass, energy, and momentum fluxes are described by the Monin-Obukhov similarity principle in CLM. The energy balance equation in CLM can be written as:

$$R_{net}(\theta) = LE(\theta) + H(\theta) + G(\theta) \tag{3}$$

where R_{net} is net radiation [Wm⁻²], LE is latent heat flux [Wm⁻²], H is sensible heat flux [Wm⁻²] ²], and G is ground heat flux [Wm⁻²]. This equation is written as a function of θ to demonstrate the connection between land surface energy balance and subsurface hydrodynamics. The source/sink term S in equation (1) corresponds to the moisture dependent LE in equation (3). The surface heat transfer in CLM is simulated by solving the heat diffusion equation. G is applied as the top boundary condition to solve this equation at the land surface and obtained as the residual of equation (3), which closes the energy balance. It should be mentioned that, CLM considers only conduction process in simulating subsurface energy transport ignoring convection, which eventually decouples the heat transport from the moisture transport in the coupled model [Kollet et al., 2009]. The land surface model CLM is forced with atmospheric variables including precipitation rate, radiation, temperature, barometric pressure, wind speed, and humidity. The off-line coupling scheme considered in this study assumes that, these atmospheric variables do not change due to transient land surface conditions [Kollet, 2009]. This assumption may influence the mass and energy fluxes simulated by the model because of the non-linear feedback mechanisms between different compartments mentioned before. Dai et al. [2001] describes the parameterizations in CLM in details.

In the coupled modeling framework, ParFlow replaces the simplified hydrological scheme in CLM and simulates subsurface hydrodynamics along with surface runoff. In return, CLM calculates the non-linear source/sink terms of soil moisture (e.g., infiltration from precipitation and *ET*, respectively) for ParFlow. At every 1h time step, the two coupled model

components exchange fluxes and shallow soil moisture distributions in an operator splitting approach.

3.3 Rur model setup

The ParFlow.CLM model is applied over a model domain encompassing the Rur catchment. A total subsurface depth of 50m is considered in the model, with a variable vertical discretization ranging from 4×10^{-2} m at the land surface to 2×10^{0} m at the bottom of the model domain using the aforementioned terrain following grid implementation. Laterally, the model has a uniform grid resolution ($\Delta x=\Delta y$) of 1km with 168 ×168 cells in x and y dimensions, respectively. No-flow lateral and bottom boundary conditions are applied to the model domain. At the land surface, a free surface overland flow boundary condition is used [*Kollet and Maxwell*, 2006].

We obtain spatially distributed vegetation cover information (Figure 2b) for the model domain from the Global Land Cover 2000 (1km spatial resolution) digital database (GLC2000, European Commission, Joint Research Centre, 2003), with plant parameters derived following the International Geosphere-Biosphere Program (IGBP) standard. The deeper subsurface in the model is homogeneous with parameter values (Table 1) obtained from *Gleeson et al.* [2011]. Digital Soil Map of the World (DSMW) provided by the Food and Agricultural Organization of UNO (FAO) and the Euro-soil database information [e.g., *Dolfing and Scheltens*, 1999] are used to represent the texture of different soil types in the shallow subsurface (Figure 2c). The van Genuchten function represents the saturation pressure head relationship for different soil types in the model [van Genuchten, 1980], with parameter values (Table 2) obtained from *Schaap and Leij* [1998].

The simulation period extends from January 2009 until December 2011 with a time resolution of one hour. Atmospheric variables are obtained from the COSMO-DE re-analysis data set of

the German Weather Service (DWD). We apply linear interpolation to downscale these atmospheric variables to the model grid resolution of 1km, because COSMO-DE operates at a lateral grid resolution of 2.8km. A model spin-up is performed to achieve a realistic initial condition. For this purpose, the model is initialized with an arbitrary uniform water table depth of 5m below ground surface. With this setup, repeated model runs are performed using the hourly atmospheric forcing data of 2009 to reach a dynamic equilibrium, which required about 20 years of simulation time.

3.4 Field measurements

The Rur catchment is the central research area for the Transregional Collaborative Research Centre, TR32 [Vereecken et al., 2010]. It is also the central monitoring site of the Eifel/Lower Rhine valley observatory of the Terrestrial Environmental Observatories, TERENO [Bogena et al., 2006], which is coordinated at the Research Centre Juelich (Forschungszentrum Juelich). This catchment has well-established measurement facilities for monitoring the mass and energy balance components from the subsurface into the atmosphere. The observations used in this study are summarized in Table 3. The geographic locations of the measurement sites are shown in Figure 2a.

River discharge measurements are obtained from the Nature, Environment, and Consumer Protection Agency (LANUV) of North Rhine-Westphalia, Germany, which collects discharge information at several gauging stations along the Rur River. There are large reservoir systems in the mountainous southern part of the catchment, which influence the downstream flow considerably. Therefore, we chose the Monschau, a gauging station at the upstream reaches of the river for comparison with the simulated discharge, which is arguably less influenced by the management practices.

A state-of-the-art wireless sensor network was installed at the forested sub-catchment Wuestebach in 2009 to gather continuous, spatially distributed soil moisture information at three different soil depths (5cm, 20cm and 50cm) [e.g., *Bogena et al.*, 2010; *Rosenbaum et al.*, 2012]. Similar sensor network was also installed at the Rollesbroich test site in 2011. We used the average soil moisture information from these sensor networks in this study. We also used the soil moisture measurements from Schoenenseiffen site, which is maintained by Research Centre Juelich. The Erftverband, a non-profit water management organization in the region provided *WTD* information at 43 observation wells located in the northern part of the catchment (Figure 2a).

Three energy balance towers were installed in 2009 at the Merken test site in different agricultural fields, namely, winter wheat, sugar beet, and barley. These towers were equipped with eddy covariance measurement instruments. *LE* and *H* data at this site were collected during TR32 FLUXPAT campaign in summer 2009 [e.g., *Graf et al.*, 2010; *Kessomkiat et al.*, 2013; *van de Boer et al.*, 2013].-These fluxes were also measured at the forested Wuestebach site in 2011. Additionally, the climate station in Merzenhausen, which is maintained by the Research Centre Juelich, has been collecting *LE* data since 2011. *R*_{net} and *G* measurements were obtained from a micrometeorological tower in Selhausen. *R*_{net} was measured at 2.5m above ground, while *G* measurements were performed at 8 cm soil depth at this site.

4. Results and discussion

4.1 Comparison to field measurements

Figure 3 shows a comparison between observed and simulated hydrographs from January 2009 through December 2011 at the Monschau discharge gauging station. The model is generally able to capture the timing of the peaks throughout the simulation period. During low flow conditions, the simulation results show good agreement with the observations. However,

the peak discharge values are underestimated in December 2010 and January 2011. The overall model performance is depicted by a Nash-Sutcliffe value [Nash and Sutcliffe, 1970] of NSE = 0.40. As mentioned earlier, the flows on the Rur River are managed with reservoir systems that are not considered by ParFlow.CLM. In order to estimate the influence of such management practices on the simulation, Figure 3 also shows the comparison between the observed and modeled hydrographs after correcting the simulated discharge by adding measured differential releases (outflow-inflow) from Perlenbach reservoir, which is located at the upstream reaches of the Monschau gauging station. This correction improves the agreement between the observed and simulated hydrographs, which is reflected by a considerably improved NSE of 0.65. Therefore, it is likely that discrepancies between the observed and simulated hydrographs result from the management practices.

Figure 4 compares the observed and simulated soil moisture at three different test sites over the Rur catchment. Simulated values for the comparison are derived by averaging the soil moisture over the top two vertical model layers. Figure 4a shows the comparison at the Wuestebach test site, demonstrating reasonable agreement between the model results and observations without model calibration. Good agreement between observed and simulated soil moisture in terms of magnitude and dynamics is observed from July to October in Figure 4a. After this period, the model becomes saturated because the porosity value used in the simulation at this location is too low [Rosenbaum et al., 2012]. Figure 4b and c compares observed and simulated soil moisture at Rollesbroich and Schoenenseiffen test sites, respectively. The dynamics in observed soil moisture due to wetting and drying is again reproduced well by the simulation. However, in both locations, the model generally underestimates soil moisture. Reasons of these discrepancies may include the uncertainty in model parameters and interpolation of the atmospheric forcing data.

Figure 5a shows a comparison between the observed and simulated *WTD* time series from January 2009 until December 2011 at 12 selected wells. The seasonal dynamics of the observed *WTD* are reproduced reasonably well by the simulation, though the model generally predicts shallower *WTD* compared to the observations. This is also observed in Figure 5b, which shows the cumulative frequency distributions of the observed and simulated mean *WTD* for all 43 wells. One possible reason for this underestimation may be the coarse lateral grid resolution of 1km, which has been discussed previously [e.g., *Zhang and Montgomery*, 1994; *Kuo et al.*, 1998; *Sulis et al.*, 2011]. As shown in Figure 2a, the 43 groundwater wells are located in the northern flat part of the catchment. Groundwater pumping in this area may lower the groundwater table [*Bogena et al.*, 2005], which may also create discrepancies between observed and simulated *WTD*. We did not attempt to correct the simulated *WTD* for pumping because reliable information on groundwater extraction is not available.

Figure 6 shows a comparison between the average daily cycles of observed and simulated LE and H in different months of 2009 at the Merken test site. The model performance is reasonable in reproducing the daily cycles of LE. The dynamics in LE are captured well throughout the measurement period with a small overestimation in mid-day during July. The daily cycle of simulated H also shows reasonable agreement with the measured data in April. However, for the rest of the measurement period, a systematic over prediction of day time H is observed. Similar results were obtained in the study by $Baker\ et\ al.\ [2005]$, where the Simple Biosphere Model (SiB2.5) overestimated H compared to eddy covariance measurements.

We apply wavelet transform to study the temporal dynamics of the observed and simulated *LE*; because interpreting the temporal variability of complex processes from direct inspection of the time series alone is not feasible. A brief description along with the mathematical formulation of the wavelet transform technique is given in Appendix A. Figure 7 show the

time-localized wavelet power and the global wavelet spectra of observed and simulated LE at the Merzenhausen test site from July 2011 through December 2011. The observed LE time series shows variability at 1day time scale due to the diurnal variation of incoming solar radiation. Additionally, monthly (about 32day time scale) variability is also observed in the measured time series. Figure 7 illustrates that the simulated time series also show variability at these two prominent time scales, which clearly demonstrates the model's capability of reproducing the dynamics in LE across different time scales. This scale dependent variability of the fluxes is the central idea behind the proposed DBF concept, which is discussed in the following section.

In addition to LE and H, we have also compared R_{net} and G measurements from the Selhausen test site with model results. These comparisons are not shown here for the sake of brevity. However, it should be mentioned that, the simulated R_{net} and G show good agreement with the observations in terms of dynamics and magnitude at daily and monthly time scales.

In our comparison of the spatially distributed mass and energy flux measurements over the Rur catchment with the simulated results, some discrepancies between observations and model results appear, which may be improved through model tuning or comprehensive model calibration. The comparisons are made between point measurements and cell-centered model grid values based on a one-km resolution. While the hydrological system is heterogeneous at all scales, we assume that cell-centered values are representative of the entire grid cells, which constitutes a major simplifying assumption. However, comparisons between observed and simulated time series based on similar assumptions have been presented previously in several useful studies related to understanding the processes in hydrological cycle [e.g., *Goderniaux et al.*, 2009; *Fan and Miguez-Macho*, 2010; *Shen et al.*, 2013].

Uncertainty in the model parameter values is expected because of the coarse grid resolution considered in this study. Various sources of uncertainty in physics-based distributed models

have been discussed in several studies [e.g., *Beven and Binley*, 1992; *Moradkhani et al.*, 2005; *Liu and Gupta*, 2007]. The influence of model parameterization on hydrological modeling results has been studied previously in connection with parameter regionalization [e.g., *Parajka et al.*, 2005; *Samaniego et al.*, 2010]. In this study, we consider pseudo-effective parameter values for each grid cell, which are based on our current best knowledge of the terrestrial system. This limitation in representing the sub grid spatial heterogeneity in the model parameter values may also contribute to discrepancies between the observed and simulated mass and energy fluxes.

The aim of this study, however, is not to perfectly reproduce the fluxes and states of the hydrological cycle in a best-fit sense. We attempt to produce reasonable model dynamics and statistics (compared to the observations) to represent processes in the coupled water and energy cycles so that the space-time variability of these processes can be analyzed. For this purpose the agreement between the observed and simulated mass and energy balance components is adequate.

4.2 Coherence in observed processes

In the previous section, we examined the variability of the observed *LE* across different time scales using the wavelet transform technique, which agrees well with the model results (Figure 7). In this section, we examine the coherence between observed *LE* and *WTD* using the cross-wavelet transform technique (Appendix A). This analysis is intended to explore the subsurface-land surface connection at different temporal scales in a time localized fashion.

Figure 8 shows the time localized cross-wavelet power of daily average measured *LE* and *WTD* time series at the Wuestebach test site. This figure shows cross-wavelet power at a monthly scale (about 32day) in summer (from June 2011 until August 2011). High cross-wavelet power is also observed at about 64day time scale. Figure 8 reveals the time localized

coherence between observed *LE* and *WTD* at two dominating time scales on the order of months in summer. This result suggests that interconnections exist between subsurface hydrodynamics and land surface processes at different time scales under moisture limited conditions, which motivates the proposed DBF concept. In the following sections we corroborate the observed coherence patterns in Figure 8 with the model results.

4.3. Analysis of simulated space-time variability

According to the DBF concept, atmosphere and groundwater act as the upper and the lower boundary conditions, respectively, for the land surface processes. As a first step, we illustrate the influence of atmospheric variability on simulated land surface processes at different time scales. Figure 9 shows the time localized wavelet power of simulated R_{net} and LE averaged over the catchment. The 1day scale variability in R_{net} spectrum is observed throughout the year, although it is less pronounced in the colder months. Additionally, R_{net} spectrum shows variability at the 32day time scale in summer. Similar to R_{net} , the wavelet power spectrum of LE shows temporal variability at 1day scale, indicating the connection between R_{net} and ET. At larger time scales, LE variability does not directly correlate with R_{net} in summer, although temporal patterns at about 32-64day are observed in the LE spectrum.

Figure 10 shows time localized wavelet power of catchment-averaged precipitation (P), simulated relative surface saturation (S_r), and simulated WTD. The P and S_r spectra show similar variability at time scales up to 8-16day throughout the year. The variability of P is reflected in S_r and WTD spectrum at about 16-32day time scale during February and September, which are the major recharge periods over the catchment. The exception is September 2010, when 16-32day variability is not visible in WTD spectrum. It should be mentioned that, 2010 is the driest of the three simulated years. This may be the reason for the discontinuity in the wavelet power spectrum of WTD, because simulated groundwater recharge dropped drastically during this time period over the catchment. Additionally,

variability in S_r spectrum at 32-64day time scale is observed in summer. These results agree with the findings of *Lauzon et al.* [2004], who demonstrated that the soil moisture data from the Orgeval watershed in France shows variability at time scales greater than 16day in summer from 1998 until 2001.

According to the DBF concept, daily LE variability (Figure 9) influences groundwater dynamics under moisture limited conditions (Figure 1, inset in WTD plot). Note that the 1day temporal pattern is visible in the WTD wavelet power spectrum in Figure 10, which is due to the daily groundwater contribution to meet ET demand under soil moisture limited conditions [e.g., Fahle and Dietrich, 2014]. Therefore, Figure 9 and 10 connect atmospheric forcing (i.e., R_{net}) and subsurface hydrodynamics to land surface energy fluxes on a 1day time scale.

Figure 11a shows the difference between simulated daily average LE_{pot} and LE over the simulation period to demonstrate the influence of moisture on ET. Significant differences between LE_{pot} and LE (LE_{pot} - LE) are observed in summer, especially in 2010. As mentioned earlier, 2010 is the driest of the three simulated years, which is the reason for the high LE_{pot} - LE observed in this year. According to the DBF concept, groundwater influences LE because of the dependence of ET on capillary rise of moisture from the free groundwater table (Figure 1). Figure 11b shows the time localized cross-wavelet power spectrum of LE_{pot} - LE and WTD to illustrate this connection. This figure shows cross-wavelet power during summer at 1day time scale, while the phase arrows indicate that the two time series generally show an antiphase relationship at this time scale. At the 32day time scale, consistent high cross-wavelet power is observed in summer. At this scale, the phase arrows show that the WTD time series slightly leads the LE_{pot} - LE time series, which demonstrates the feedback of WTD variability on summer ET at this time scale. In 2010 and 2011, significant wavelet power at the time scales greater than 64day suggests that under dry conditions, coherence between LE_{pot} - LE and WTD is extended to larger time periods.

The wavelet transform analysis above correlates the mass and energy balance components across different time scales using the catchment-averaged time series in the context of DFB concept. In order to demonstrate the coherence between the spatial patterns of these processes, we present log-log unit semivariograms (i.e., power spectra [e.g., *Wen and Sinding-Larsen*, 1997; *Gneiting et al.*, 2012]) of simulated LE, WTD, and R_{net} in summer and winter over the Rur catchment in Figure 12. Note that these semivariograms are based on the average summer and winter time fluxes over the three simulated years (2009-2011).

The unit semivariogram of R_{net} does not exhibit a clear sill within the length scale of the catchment in summer or winter. This indicates that the spatial structure of R_{net} either follows a power law behavior or a large-scale stationary process with a correlation scale larger than the catchment. While the unit semivariogram of WTD shows spatial correlation for scales less than 5km throughout the year, the LE semivariogram exhibits strong seasonal dependence. In summer, the unit semivariogram of LE shows similar spatial pattern to that of WTD, with correlation for scales less than 5km. During winter, on the contrary, the semivariogram of LE shows similar behavior to that of R_{net} with monotonically increasing semivariance and without a distinct sill within the length scale of the catchment.

The cross-semivariograms in Figure 13 demonstrate the spatial coherence between *LE* and *WTD* in summer and winter. Under soil moisture limited conditions (summer), the *LE* and *WTD* are negatively correlated for scales less than 5km, which agrees well with the univariate semivariograms for these variables (Figure 12). In winter, on the other hand, *LE* and *WTD* show weaker positive correlation and the cross-semivariogram does not exhibit a clear sill within the length scale of the catchment.

According to the proposed DBF concept, the groundwater influence on ET is observed under soil moisture limited conditions. The variogram analysis illustrates groundwater and atmospheric forcing control on the spatial pattern of LE in summer and winter, respectively.

The negative correlation between LE and WTD in Figure 13 demonstrates the interconnection between the spatial patterns of groundwater and ET under dry conditions. This negative correlation exists due to higher ET at locations with shallower groundwater table depth and vice-versa, which suggests the groundwater control on the spatial pattern of summer ET. In winter, LE semivariogram shows similar behavior to that of R_{net} (Figure 12) because of the prevailing energy limited conditions over the catchment during the colder months of the year.

5. Summary and conclusions

In this study, the concept of the *dual-boundary forcing* (DBF) is proposed to describe and quantify the feedback mechanisms between different compartments of the hydrological cycle in space and time. According to the proposed DBF concept, the atmosphere and groundwater act as the upper and lower boundary conditions, respectively, for land surface processes. These boundary conditions influence the land surface at different space-time scales. The availability of energy and moisture determines the dominating boundary condition for the exchange processes.

The coupled subsurface-land surface model ParFlow.CLM was applied on the Rur catchment, Germany, and the space-time patterns of the mass and energy fluxes were analyzed using wavelet transform and variogram techniques to verify this concept. Prior to this analysis, a comparison between the model results and observations was performed, which shows reasonable agreement for different mass and energy fluxes even without comprehensive model calibration. While uncertainties in the simulation results may arise from model structure, parameters, and atmospheric forcing data, ParFlow.CLM is forced by re-analysis datasets from COSMO-DE and ensures closure of the mass and energy balances resulting in an internally consistent description of the relevant process, system dynamics and feedbacks.

The results suggest that at the daily time scale, ET variability is driven by the radiative atmospheric forcing (R_{net}). This variability of ET influences the subsurface hydrodynamics and creates the diurnal WTD fluctuation through daily water uptake under moisture limited conditions, which is analogous to periodic pumping of groundwater. Groundwater storage, on the other hand, depletes due to this withdrawal and influences ET mainly at the monthly time scale under moisture limited conditions in summer. It was also demonstrated that this influence extends to multi-month time scales in dry periods.

It should be mentioned that the groundwater control on *ET* may be significant at even longer time scales due to the long term memory effect of subsurface hydrodynamics under e.g., prolonged drought conditions. This influence was not considered here due to data limitation, because the simulation was performed and compared to measured data over three years (2009-2011). However, this effect can also be interrogated utilizing the proposed techniques with extended time series of fluxes and states, which is planned in future.

The variogram analysis demonstrates the seasonal dependence of spatial variability of ET. Under energy limited conditions, the spatial pattern of ET is determined by R_{net} . Strong influence of groundwater on the spatial variability of ET is observed under moisture limited conditions. These findings suggest that, water table observations are useful in predicting the spatial pattern of ET in summer. In winter, however, the spatial pattern of ET may be predicted from R_{net} measurements alone (e.g., from remote sensing observations).

It has been discussed earlier that the simulation results may be affected by the coupled model structure, grid resolution, parameterization, and interpolation of atmospheric forcing data. There is a need of a comprehensive sensitivity and uncertainty analysis study to assess the impact of the aforementioned issues on DBF concept, which would require novel, non-traditional approaches and large computer resources. This is beyond the scope of the current study and should be the subject of future research.

Acknowledgements

We gratefully acknowledge the support by the CRC/TR32 project "Patterns in Soil-Vegetation-Atmosphere Systems: Monitoring, Modelling and Data Assimilation" funded by the German Research Foundation (DFG). The TERENO data used in this study are freely available via the online data portal TEODOOR (http://teodoor.icg.kfa-juelich.de/). We would like to thank Clemens Drüe (University of Trier, Germany) for providing the eddy covariance measurements at Wuestebach test site. The outflow data from Perlenbach reservoir is obtained from Wasserwerk-Perlenbach website (http://www.wasserwerk-perlenbach.de/). The Matlab scripts used to perform the continuous wavelet transform analysis were originally written by A. Grinsted. We would like to thank the Associate Editor Luis Samaniego and the three anonymous reviewers for their comments and suggestions, which added to the quality of this manuscript. We are also grateful to John Williams for his valuable comments related to this manuscript.

Appendix A

A.1 Variogram analysis

In this study, the spatial variability of different fluxes in the coupled water and energy cycles are analyzed using semivariograms. According to *Goovaerts* [1997], the experimental semivariogram for a spatially distributed attribute z is calculated as

$$\gamma(h) = \frac{1}{2N(h)} \sum_{\alpha=1}^{N(h)} [z(u\alpha) - z(u\alpha + h)]^2$$

where h is the lag distance, N is the number of pairs, and u is measurement location. The cross-semivariogram between z_a and z_b is calculated as

$$\gamma_{ab}(h) = \frac{1}{2N(h)} \sum_{\alpha=1}^{N(h)} \left[z_a(u\alpha) - z_a(u\alpha + h) \right] \left[z_b(u\alpha) - z_b(u\alpha + h) \right]$$

In this study, we calculate omni-directional variograms, which assumes that the data is isotropic.

A.2 Continuous wavelet transform analysis

The wavelet transform is a useful tool in analyzing time series variability and has been used previously to analyze various geophysical data [e.g., *Andreo et al.*, 2006; *Liu et al.*, 2011; *Perez-Valdivia et al.*, 2012]. We use continuous wavelet transform analysis to show the time localized temporal variance of different processes as a function of frequency. If x_n is a timeseries ($n = 0 \dots N-1$) with an equal time spacing of δt , according to *Torrence and Compo* [1997], the continuous wavelet transform of x_n can be defined as its convolution with a scaled and translated version of a wavelet function $\psi_0(\eta)$

$$W_n(s) = \sum_{n'=0}^{N-1} x_n \psi_0 * \left[\frac{(n'-n)\delta t}{s} \right]$$

where s is the wavelet scale and (*) denotes the complex conjugate. The wavelet function depends on the non-dimensional time parameter η . In this study, we use the Morlet wavelet as the wavelet function, which can be expressed as

$$\psi_0(\eta) = \pi^{-1/4} e^{i\omega_0 \eta} e^{-\eta^2/2}$$

where ω_0 is the non-dimensional frequency. The global wavelet power is obtained by averaging the wavelet powers over the localized time instances and can be defined as

$$\overline{W}^{2}(s) = \frac{1}{N} \sum_{n=0}^{N-1} |W_{n}(s)|^{2}$$

The cross-wavelet spectrum of two time series x and y can be defined as

$$W_n^{xy} = W_n^x(s)W_n^y *(s)$$

where $W_n^x(s)$ and $W_n^y(s)$ denote the wavelet transform of x and y, respectively. According to *Torrence and Compo* [1997], high cross-wavelet power indicates covariance between the time series. *Grinsted et al.* [2004] argued that a phase locked phenomenon with high cross-wavelet power implies a cause and effect relationship between two time series.

References

- Amenu, G. G., and P. Kumar (2005), Interannual variability of deep-layer hydrologic memory and mechanisms of its influence on surface energy fluxes, J. Climate, 18, 5024-5040.
- Andreo, B., P. Jimenez, J. J. Duran, F. Carrasco, I. Vadillo, and A. Mangin (2006), Climatic and hydrological variations during the last 117–166 years in the south of the Iberian Peninsula, from spectral and correlation analyses and continuous wavelet analyses, J. Hydrol., 324, 24-39.
 - Anyah, R. O., C. P. Weaver, G. Miguez-Macho, Y. Fan, and A. Robock (2008), Incorporating water table dynamics in climate modeling; 3. Simulated groundwater influence on coupled land-atmosphere variability, J. Geophys. Res., 113, D07103, doi:10.1029/2007JD009087.
 - Ashby, S. F., and R. D. Falgout (1996), A parallel multigrid preconditioned conjugate gradient algorithm for groundwater flow simulations, Nucl. Sci. Eng., 124(1), 145–159.
 - Baker, I., A. S. Denning, N. Hanan, L. Prihodko, M. Uliasz, P.-L. Vidale, K. Davis, and P. Bakwin (2003), Simulated and observed fluxes of sensible and latent heat and CO2 at the WLEF-TV tower using SiB2.5, Glob. Change Biol., 9, 1262–1277.
 - Beecham, S., and R. K. Chowdhury (2010), Temporal characteristics and variability of point rainfall: a statistical and wavelet analysis, Int. J. Climatol., 30, 458–473.
 - Betts, A. K., J. H. Ball, A. C. M. Beljaars, M. J. Miller, and P. A. Viterbo (1996), The land-atmosphere interaction: A review based on observational and global modeling perspectives, J. Geophys. Res., 101(D3), 7209-7225.
 - Beven, K., and A. Binley (1992), The future of distributed models: Model calibration and uncertainty prediction, Hydrol. Process., 6, 279-298.

Bogena, H. R., K. Schulz, and H. Vereecken (2006), Towards a network of observatories in terrestrial environmental research, Adv. Geosci., 9, 109-114.

Bogena, H. R., M. Herbst, J. A. Huisman, U. Rosenbaum, A. Weuthen, and H. Vereecken (2010), Potential of wireless sensor networks for measuring soil water content variability, Vadise Zone J., 9, 1002-1013.

Bogena, H., M. Herbst, J.-F. Hake, R. Kunkel, C. Montzka, Th. Puetz, H. Vereecken, and F. Wendland (2005), "MOSYRUR - Water balance analysis in the Rur basin,"

Forschungszentrum Juelich, ISBN 3-89336-385-8.

Brubaker, K. L., and D. Entekhabi (1996), Analysis of feedback mechanisms in landatmosphere interaction, Water Resour. Res., 32, 1343-1357.

Chen, X., and Q. Hu (2004), Groundwater influences on soil moisture and surface evapotration, J. Hydrol., 297, 285-300.

Dai, X. P., X. Zeng, and C. D. Dickinson (2001), The Common Land Model (CLM): Technical documentation and user's guide.

Dai, Y. J., et al. (2003), The Common Land Model, Bull. Am. Meteorol. Soc., 84(8), 1013–1023.

Delworth, T., and S. Manabe (1988), Climate variability and land-surface processes, Adv. Water Resour., 1, 523-547.

Ding, R., S. Kang, R. Vargas, Y. Zhang, X. Hao (2013), Multiscale spectral analysis of temporal variability in evapotranspiration over irrigated croplands in arid region, Agric. Water Manage., 130, 79-89.

Dolfing, J., and S. D. Scheltens (1999), Facilitated transport in European soils from the Eurosoil project, Env. Toxicol. Chem., 18(7), 1417-1420.

Fahle, M., and O. Dietrich (2014), Estimation of evapotranspiration using diurnal groundwater level fluctuation: Comparison of different approaches with groundwater lysimeter data, Water Resour. Res., 50, 273-286, doi:10.1002/2013WR014472.

Fan, Y., and G. Miguez-Macho (2010), Potential groundwater contribution to Amazom evapotranspiration, Hydrol. Earth Syst. Sci., 14, 2039–2056, doi:10.5194/hess-14-2039-2010.

Ferguson, C. R., and E. F. Wood (2011), Observed land-atmospheric coupling from satellite remote sensing and reanalysis, J. Hydrometeorol., 12, 1221-1254, doi: 10.1175/2011JHM1380.1.

Fernández-Prieto, D., J. Kesselmeier, M. Marconcini, A. Reissell, and T. Suni (2013), Earth observation for land-atmosphere interaction science, Biogeosciences, 10, 261–266.

Findell, K. L., and E. A. B. Eltahir (1997), An analysis of the soil moisture-rainfall feedback, based on direct observations from Illinois, Water Resour. Res., 33(4), 725-735.

Gedney, N., and P. M. Cox (2003), The sensitivity of global climate model simulations to the representation of soil moisture heterogeneity, J. Hydrometeorol., 4, 1265-1275.

Gleeson, T., L. Smith, N. Moosdorf, J. Hartmann, H. H. Duerr, A. H. Manning, L. P. H. van Beek, and A. M. Jellinek (2011), Mapping permeability over the surface of the Earth, Geophys. Res. Let., 38, L02401, doi:10.1029/2010GL045565.

Gneiting, T., H. Ševčiková, and D. B. Percival, Estimators of fractal dimension: Assessing the roughness of time series and spatial data, Statis. Sci., 27(2), 247-277, doi: 10.1214/11-STS370.

Goderniaux, P., S. Brouyère, H. J. Fowler, S. Blenkinsop, R. Therrien, P. Orban, and Alain Dassargues (2009), Large scale surface-subsurface hydrological model to assess climate change impacts on groundwater reserves, J. Hydrol., 373, 122-138.

Goovaerts, P., (1997) Geostatistics for natural resources evaluation, Oxford University Press New York, 496pp.

Graf, A., D. Schüttemeyer, H. Geiß, A. Knaps, M. Möllmann-Coers, J. H. Schween, S. Kollet, B. Neininger, M. Herbst, H. Vereecken (2010), Boundedness of turbulent temperature probability distributions and their relation to the vertical profile in the convective boundary layer, Bound. Layer Meteorol., 134, 459–486.

Gribovszki, Z., J. Szilágye, and P. Kalicz (2010), Diurnal fluctuations in shallow groundwater levels and streamflow rates and their interpretation – A review, J. Hydrol., 385, 371-383.

Grinsted, A., J. C. Moore, and S. Jevrejeva (2004), Application of the cross wavelet transform and wavelet coherence to geophysical time series, Nonlin. Process. Geophys., 11, 561-566.

Gundogdu, K. S., and I. Guney (2007), Spatial analysis of groundwater levels using universal kriging, J. Earth Syst. Sci., 116(1), 49-55.

Haddad, Z. S., J. P. Meagher, R. F. Adler, E. A. Smith, E. Im, and S. L. Durden (2004), Global variability of precipitation according to the tropical rainfall measuring mission, J. Geophys. Res., 109, doi:10.1029/2004JD004607.

Hsu, K.-C., and S.-T. Li (2010), Clustering spatial-temporal precipitation data using wavelet transform and self-organizing map neural network, Adv. Water Resour., 33, 190-200.

Jones, J. E., and C. S. Woodward (2001), Newton-Krylov-multigrid solvers for large-scale, highly heterogeneous, variably saturated flow problems, Adv. Water Resour., 24(7), 763–774.

Kessomkiat, W., H.-J. Franssen, A. Graf, and H. Vereecken (2013), Estimating random errors of eddy covariance data: An extended two-tower approach, Agric. Forest Meteorol., 171-172, 203-219.

Kollet, S. J. (2009), Influence of soil heterogeneity on evapotranspiration under shallow water table conditions: transitent, stochastic simulations, Environ. Res. Lett., 4, doi:10.1088/1748-9326/4/3/035007.

Kollet, S. J., and R. M. Maxwell (2006), Integrated surface-groundwater flow modeling: A free-surface overland flow boundary condition in a parallel groundwater flow model, Adv. Water Resour., 29(7), 945–958.

Kollet, S. J., and R. M. Maxwell (2008), Capturing the influence of groundwater dynamics on land surface processes using an integrated, distributed watershed model, Water Resour. Res., 44, W02402, doi:10.1029/2007WR006004.

Kollet, S. J., I. Cvijanovic, D, Schüttermeyer, R. M. Maxwell, A. F. Moene, and P. Bayer (2009), The influence of rain sensible heat and subsurface energy transport on the energy balance at the land surface, Vadose Zone J., 8, 846-857, doi:10.2136/vzj2009.0005.

Kumar, P., and E. F. Georgiou (1993), A multicomponent decomposition of spatial rainfall fields 1. Segregation of large- and small-scale features using wavelet transforms, Water Resour. Res., 29(8), 2515-2532.

Kuo W.-L., T. S. Steenhuis, C. E. McCulloch, C. L. Mohler, D. A. Weinstein, S. D. DeGloria, and D. P. Swaney (1999), Effect of grid size on runoff and soil moisture for a variable-source-area hydrology model. Water Resour. Res., 35(11), 3419–3428.

Labat, D., J. Ronchail, and J. L. Guyot (2005), Recent advances in wavelet analyses: Part2-Amazon, Parana, Orinoco and Congo discharges time scale variability, J. Hydrol., 314, 289-311.

Lam, A., D. Karssenberg, B. J. J. M. van den Hurk, and M. F. P. Bierkens (2011), Spatial and temporal connections in groundwater contribution to evaporation, Hydrol. Earth Syst. Sci., 15, 2621–2630.

Lauzon, N., F. Anctil, and J. Petrinovic (2004), Characterization of soil moisture conditions at temporal scales from a few days to annual, Hydrol. Process., 18, 3235-3254, doi: 10.1002/hyp.5656.

Liang, X., and Y.-K. Zhang (2013), Temporal and spatial variation and scaling of groundwater levels in a bounded unconfined aquifer, J. Hydrol., 479, 139-145.

Liang, X., Z. Xie, and M. Huang (2003), A new parameterization for surface and groundwater interactions and its impact on water budgets with the variable infiltration capacity (VIC) land surface model, J. Geophys. Res., 108(D16), doi:10.1029/2002JD003090.

Little, M. A., and J. P. Bloomfield (2010), Robust evidence for random fractal scaling of groundwater levels in unconfined aquifers, J. Hydrol., 393, 362-369.

Liu, H.-L., A.-M. Bao, X. Chen, L. Wang, and X.-L. Pan (2011), Response analysis of rainfall–runoff processes using wavelet transform: a case study of the alpine meadow belt, Hydrol. Process., 25, 2179-2187.

Liu. Y., and H. V. Gupta (2007), Uncertainty in hydrologic modeling: Towards an integrated data assimilation framework, Water Resour. Res., 43, W07401, doi:10.1029/2006WR005756.

Manabe, S., and T. Delworth (1990), The temporal variability of soil wetness and its impact on climate, *Climate Change*, *16*, 185-192.

Matsoukas, C., S. Islam, and I. Rodriguez-Iturbe (2000), Detrended fluctuation analysis of rainfall and streamflow time series, J. Geophys. Res., 105, D23, 29165-29172.

Maxwell, R. M. (2013), A terrain-following grid transform and preconditioner for parallel, large-scale integrated hydrologic modeling, Adv. Water Resour., 53, 109-117.

Maxwell, R. M., and N. L. Miller (2005), Development of a coupled land surface and groundwater model, J. Hydrometeorol., 6, 233-247.

Maxwell, R. M., F. K. Chow, and S. J. Kollet (2007), The groundwater-land-surface-atmosphere connection; Soil moisture effects on the atmospheric boundary layer in fully-coupled simulations, Adv. Water Resour., 30, 2447-2466.

Miguez-Macho, G., and Y. Fan (2012a), The role of groundwater in the Amazon water cycle: 1. Influence on seasonal streamflow, flooding and wetlands, J. Geophys. Res., 117, D15113, doi:10.1029/2012JD017539.

Miguez-Macho, G., and Y. Fan (2012b), The role of groundwater in the Amazon water cycle: 2. Influence on seasonal soil moisture and evapotranspiration, J. Geophys. Res., 117, D15114, doi:10.1029/2012JD017540.

Moradkhani, H., K.-L. Hsu, H. Gupta, and S. Sorooshian (2005), Uncertainty assessment of hydrologic model states and parameters: Sequential data assimilation using the particle filter, Water Resour. Res., 41, W05012.

Nash, J. E., and J. V. Sutcliffe (1970), River flow forecasting through conceptual models Part I – A discussion of principles, J. Hydrol., 10, 282-290.

Niu, G.-Y., C. Paniconi, P. A. Troch, R. L. Scott, M. Durcik, X. Zeng, T. Huxman, and D. C. Goodrich (2013), An integrated modelling framework of catchment-scale ecohydrological processes: 1. Model description and tests over an energy-limited watershed, Ecohydrol., doi: 10.1002/eco.1362.

Parajka, J., R. Merz, and G. Blöschl (2005), A comparison of regionalisation methods for catchment model parameters, Hydrol. Earth Syst. Sci., 9, 157-171.

Perez-Valdivia, C., D. Sauchyn, and J. Vanstone (2012), Groundwater levels and teleconnection patterns in the Canadian Prairies, Water Resour. Res., 48, W07516, doi:10.1029/2011WR010930.

Phillips, T. J., and S. A. Klein (2014), Land atmosphere coupling manifested in warm-season observations on the U.S. southern great plains, J. Geophys. Res. Atmos., 119, 509–528, doi:10.1002/2013JD020492.

Porporato, A., P. D'Odorico, L. Ridolfi, and I. Rodriguez-Iturbe (2000), A spatial model for soil-atmosphere interaction: Model construction and linear stability analysis, *Am. Met. Soc.*, *1*, 61-74.

Richards, L. A. (1931), Capillary conduction of liquids through porous mediums, Physics 1, 318, doi: 10.1063/1.1745010.

Rosenbaum, U., H. R. Bogena, M. Herbst, J. A. Huisman, T. J. Peterson, A. Weuthen, A. W. Western, and H. Vereecken (2012), Seasonal and event dynamics of spatial soil moisture patterns at the small catchment scale, Water Resour. Res., 48, W10544, doi:10.1029/2011WR011518.

Rowell, D. P., and C. Blondin (1990), The influence of soil wetness distribution on short-range rainfall forcasting in the West African Sahel, Q. J. R. Meteorol. Soc, 116, 1471-1485.

Samaniego, L., R. Kumar, and S. Attinger (2010), Multiscale parameter regionalization of a grid-based hydrologic model at the mesoscale, Water Resour. Res., 46, W05523, doi:10.1029/2008WR007327.

Schaap, M. G., and F. J. Leij (1998), Database-related accuracy and uncertainty of pedotransfer functions, Soil Sci., 163(10), 765–779.

Schilling, K. E., and Y.-K. Zhang (2012), Temporal scaling of groundwater level fluctuations near a stream, Ground Water, 50(1), 59-67.

Seneviratne, S.I., and R. Stöckli (2008), in: Bronnimann, S., J. Luterbacher, T. Ewen, H.F. Diaz, R.S. Stolarski, U. Neu (Eds.), Climate Variability and Extremes during the Past 100 Years, Series: Adv. Global Change Research, vol. 33, Springer, Dordrecht, pp. 179–193.

Seuffert, G., P. Gross, and C. Simmer (2002), The influence of hydrologic modeling on the predicted local weather: Two-way coupling of a mesoscale weather prediction model and a land surface hydrologic model, J. Hydrometeorol., 3, 505-523.

Shen, C., J. Niu, and M. S. Phanikumar (2013), Evaluating controls on coupled hydrologic and vegetation dynamics in a humid continental climate watershed using a subsurface-land surface processes model, Water Resour. Res., 49, doi:10.1002/wrcr.20189.

Sklash, M. G., and R. N. Farvolden (1979), The role of groundwater in storm runoff, J. Hydrol., 43, 45-65.

Smith, L. C., D. L. Turcotte, and B. L. Isacks (1998), Stream flow characterization and feature detection using a discrete wavelet transform, Hydrol. Process., 12, 233-249.

Soylu, M. E., E. Istanbulluoglu, J. D. Lenters, and T.Wang (2011), Quantifying the impact of groundwater depth on evapotranspiration in a semi-arid grassland region, Hydrol. Earth Syst. Sci., 15, 787–806.

Sulis, M., C. Paniconi, and M. Camporese (2011), Impact of grid resolution on the integrated and distributed response of a coupled surface–subsurface hydrological model for the des Anglais catchment, Quebec, Hydrol. Proc., 25, 1853-1865.

Szilagyi, J., V. A. Zlotnik, and J. Jozsa (2013), Net recharge vs. depth to groundwater relationship in the platte river valley of Nebraska, United States, Groundwater, 51(6), 945-951.

Táany, R. A., A. B. Tahboub, and G. A. Saffarini (2009), Geostatistical analysis of spatiotemporal variability of groundwater level fluctuations in Amman-Zarqa basin, Jordan: a case study, Environ. Geol., 57, 525-535.

Tian, W., X. Li, G.-D. Cheng, X.-S. Wang, and B. X. Hu (2012), Coupling a groundwater model with a land surface model to improve water and energy cycle simulation, Hydrol. Earth Syst. Sci., 16, 4707–4723, doi:10.5194/hess-16-4707-2012.

Torrence, C., and G. P. Compo (1997), A practical guide to wavelet analysis, Bul. Am. Met. Soc., 79(1), 61-78.

van de Boer, A., A.F. Moene, D. Schüttemeyer, A. Graf (2013), Sensitivity and uncertainty of analytical footprint models according to a combined natural tracer and ensemble approach, Agric. For. Meteorol., 169, 1–11.

van Genuchten, M. Th. (1980), A closed-form equation for predicting the hydraulic conductivity of unsaturated soils, Soil Sci. Soc. Am. J., 44,892-898.

Vereecken, H., S. Kollet, and C. Simmer (2010), Patterns in Soil–Vegetation–Atmosphere systems: Monitoring, modeling, and data assimilation, Vadose Zone J., 9, 821-827.

Vrugt, J. A., C. G. H. Diks, H. V. Gupta, W. Bouten, and J. M. Verstraten (2005), Improved treatment of uncertainty in hydrologic modeling: Combining the strengths of global optimization and data assimilation, Water Resour. Res., 41, W01017, doi:10.1029/2004WR003059.

Wen, R., and R. Sinding-Larsen (1997), Uncertainty in fractal dimension estimated from power spectra and variograms, Math. Geol., 29(6), 727-753.

Wu, W., and R. E. Dickinson (2004), Time scales of layered soil moisture memory in the context of land-atmosphere interaction, J. Climate, 17, 2752-2764.

Yeh, P. J.-F, and E. A. B. Eltahir (2005), Representation of water table dynamics in a land surface scheme. Part I: model development, J. Climate, 18, 1861-1880.

York, J. P., M. Person, W. J. Gutowski, and T. C. Winter (2002), Putting aquifers into atmospheric simulation models: An example from the Mill Creek Watershed, northeastern Kansas, Adv. Water Resour., 25(2), 221–238.

Yuan, X., Z. Xie, J. Zheng, X. Tian, and Z. Yang (2008), Effects of water table dynamics on regional climate: A case study over east Asian monsoon area, J. Geophys. Res., 113, D21112, doi:10.1029/2008JD010180.

Zhang W., and D. R. Montgomery (1994), Digital elevation model grid size, landscape representation, and hydrologic simulation, Water Resour. Res., 30(4), 1019–1028.

Zhang, J., W.-C. Wang, and J. Wei (2008), Assessing land-atmosphere coupling using soil moisture from the Global Land Data Assimilation System and observational precipitation, J. Geophys. Res., 113, D17119, doi:10.1029/2008JD009807.

List of Tables

Table 1. Soil hydraulic parameters of the homogeneous deep subsurface.

Table 2. Soil hydraulic parameters of shallow subsurface.

Table 3. Location, temporal extent, measurement frequency, and source of the field measurements.

List of Figures

- Figure 1. Schematic of the proposed *dual boundary forcing* (DBF) concept. Hypothetical time series of atmospheric (R_{net}), land surface (LE), and subsurface (WTD) processes are partitioned based on the energy and moisture availability. The shaded area in each plot indicates the energy limited period. The inset in WTD time series shows the high frequency variability of subsurface hydrodynamics under moisture limited conditions.
- Figure 2. Location and topography (a), vegetation cover (b), and soil texture (c) information of the Rur catchment. The blue lines and the legends on the topography show the river network and the locations of the measurement stations, respectively.
- Figure 3. Precipitation (top) and observed and simulated hydrographs (bottom) at the Monschau discharge gauging station. The *corrected* discharge is calculated by adding measured differential releases (outflow-inflow) from the Perlenbach reservoir to the simulated data.
- Figure 4. Observed and simulated soil moisture at Wuestebach (a), Rollesbroich (b), and Schoenenseiffen (c) test sites.
 - Figure 5. Observed and simulated groundwater table depth, *WTD* time series at 12 selected groundwater wells (a), and cumulative frequency distributions of the observed and simulated *WTD* (b).
- Figure 6. Observed and simulated average daily cycles of latent heat flux, LE, and sensible heat flux, H at the Merken test site. The solid black lines show the mean values of simulated data. The red lines and shaded areas show the mean and standard deviation of observed flux, respectively.

- Figure 7. Wavelet transform of observed and simulated latent heat flux, LE, at the Merzenhausen test site. The time localized power is shown in the left panels. The cone of influence is indicated with the thick black lines in these plots. The right panels show the global wavelet power.
- Figure 8. Time localized cross-wavelet power of daily average observed latent heat flux, *LE*, and groundwater table depth, *WTD* time series at the Wuestebach test site.
- Figure 9. Time localized wavelet power of net radiation, R_{net} , and latent heat flux, LE.
- Figure 10. Time localized wavelet power of Precipitation, P, relative surface saturation, S_r , and groundwater table depth, WTD. The enlarged part of WTD spectrum (from January 2010 until December 2011) shows the power with small amplitude at 1-4.5day time scale.
- Figure 11. Difference between daily average simulated potential and actual latent heat flux, LE_{pot} LE (a), and time localized cross-wavelet power of LE_{pot} LE and water table depth, WTD, over the simulation period. The arrows show the phase relationship between the two time series (right arrow: in phase; left arrow: anti-phase; up arrow: LE_{pot} LE is leading by 90°; and down arrow: WTD is leading by 90°).
- Figure 12. Unit semivariograms of latent heat flux, LE, groundwater table depth, WTD, and net radiation, R_{net} in summer and winter. Note the log-log scale.
- Figure 13. Cross-semivariograms of latent heat flux, *LE*, and groundwater table depth, *WTD* in summer and winter. Note the dual y-axis.

Tables

Table 1. Soil hydraulic parameters of the homogeneous deep subsurface.

	Parameter name	Parameter value	Unit
S	aturated hydraulic conductivity, k_{sat}	6.4×10^{-6}	ms ⁻¹
	Porosity, ϕ	0.44	-
	van Genuchten parameter, α	2.1	m^{-1}
	van Genuchten parameter, <i>n</i>	3.0	-
	Residual saturation, S_{res}	0.1	-

Table 2. Soil hydraulic parameters of shallow subsurface.

Texture	K_{sat} [ms ⁻¹]	φ	$\alpha[\mathbf{m}^{\text{-1}}]$	n	S_{res}
Silty clay	8.3×10 ⁻⁷	0.389	2.7	2.0	0.2
Silt loam	3.9×10^{-6}	0.441	2.1	3.0	0.1
Clay loam	1.1×10^{-6}	0.354	2.1	2.0	0.15

Table 3. Location, temporal extent, measurement frequency, and source of the field measurements.

Data	Location	Temporal extent	Frequency	Source
Discharge	Monschau	01.01.2009 - 31.12.2009	Daily	LANUV
Soil moisture	Wuestebach	01.07.2009 - 31.12.2009	15 min	TERENO
Soil moisture	Rollesbroich	05.05.2011 - 31.12.2011	15 min	TERENO
Soil moisture	Schoenenseiffen	01.01.2010 - 31.12.2011	10 min	TERENO
Water table depth	_*	01.01.2009 - 31.12.2009	Weekly - Monthly	LANUV
Water table depth	Wuestebach	01.01.2011 - 31.12 2011	Daily	TERENO
Latent heat flux	Merken	01.04.2009 - 31.08.2009	30 min	TR32 database
Latent heat flux	Wuestebach	18.02.2011 - 31.12.2011	30 min	Uni. Trier
Latent heat flux	Merzenhausen	01.07.2011 - 31.12.2011	30 min	TERENO
Sensible heat flux	Merken	01.04.2009 - 31.08.2009	30 min	TR32 database
Net radiation	Selhausen	01.01.2009 - 31.12.2009	60 min	TERENO
Ground heat flux	Selhausen	01.01.2009 - 31.12.2009	60 min	TERENO

^{*} The locations are shown in Figure 2a

Figures

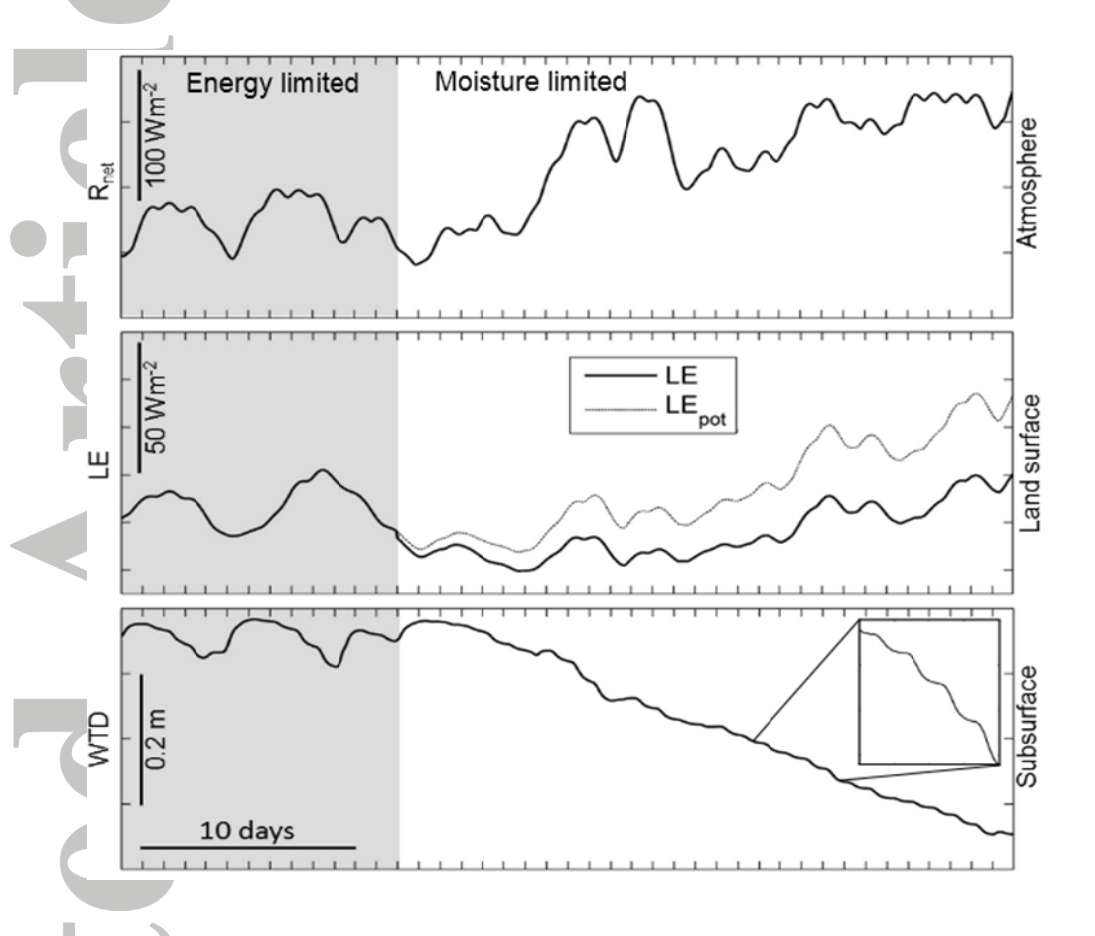


Figure 1. Schematic of the proposed *dual boundary forcing* (DBF) concept. Hypothetical time series of atmospheric (R_{net}), land surface (LE), and subsurface (WTD) processes are partitioned based on the energy and moisture availability. The shaded area in each plot indicates the energy limited period. The inset in WTD time series shows the high frequency variability of subsurface hydrodynamics under moisture limited conditions.



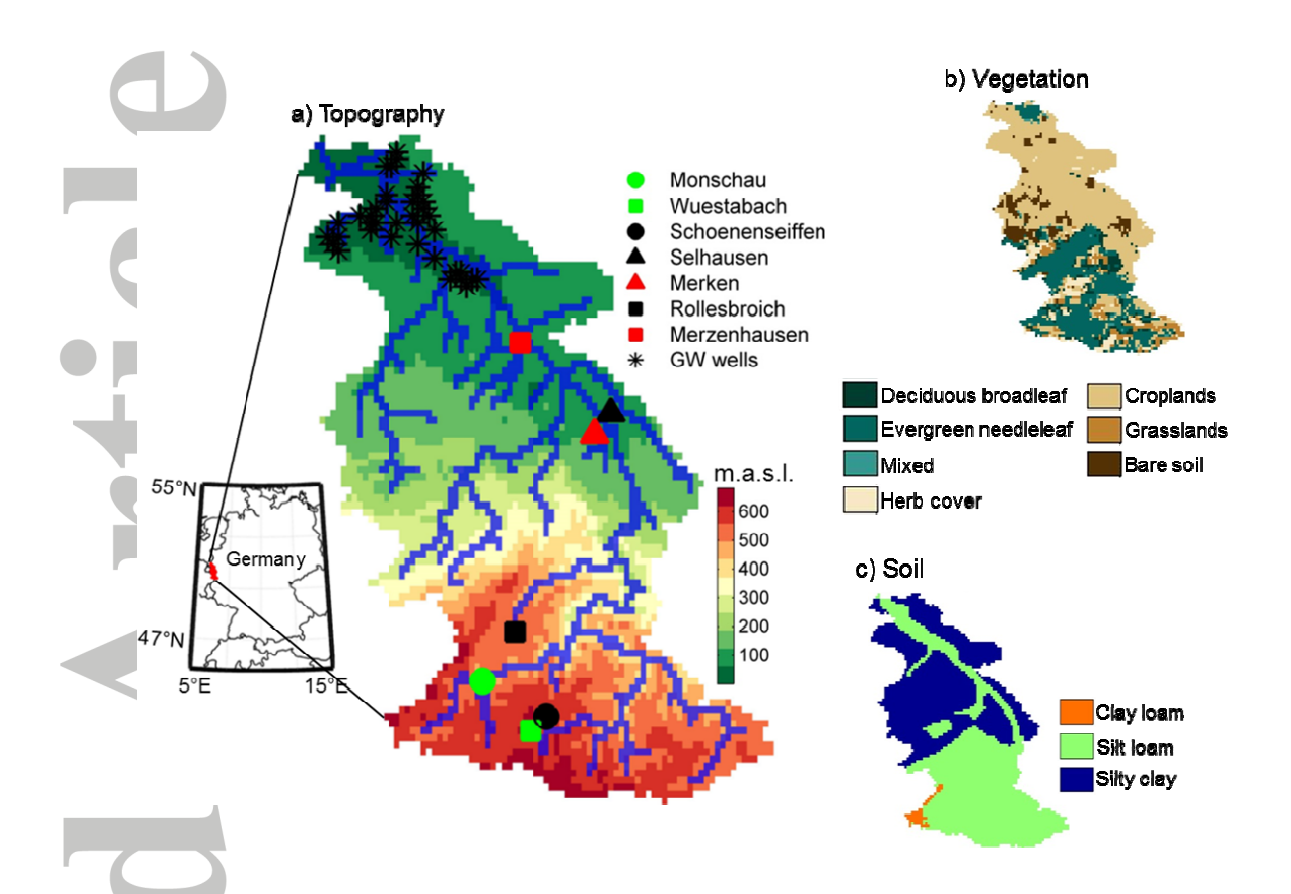


Figure 2. Location and topography (a), vegetation cover (b), and soil texture (c) information of the Rur catchment. The blue lines and the legends on the topography show the river network and the locations of the measurement stations, respectively.

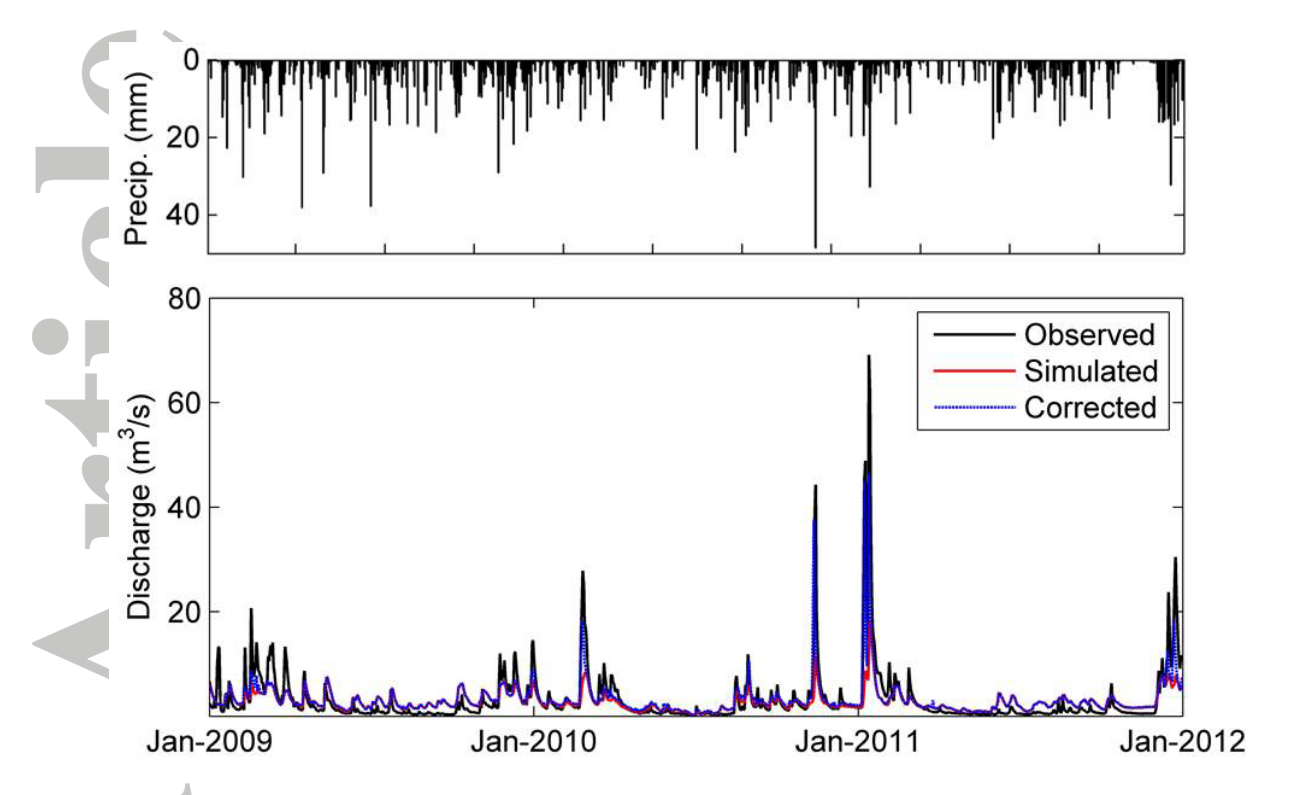


Figure 3. Precipitation (top) and observed and simulated hydrographs (bottom) at the Monschau discharge gauging station. The *corrected* discharge is calculated by adding measured differential releases (outflow-inflow) from the Perlenbach reservoir to the simulated data.

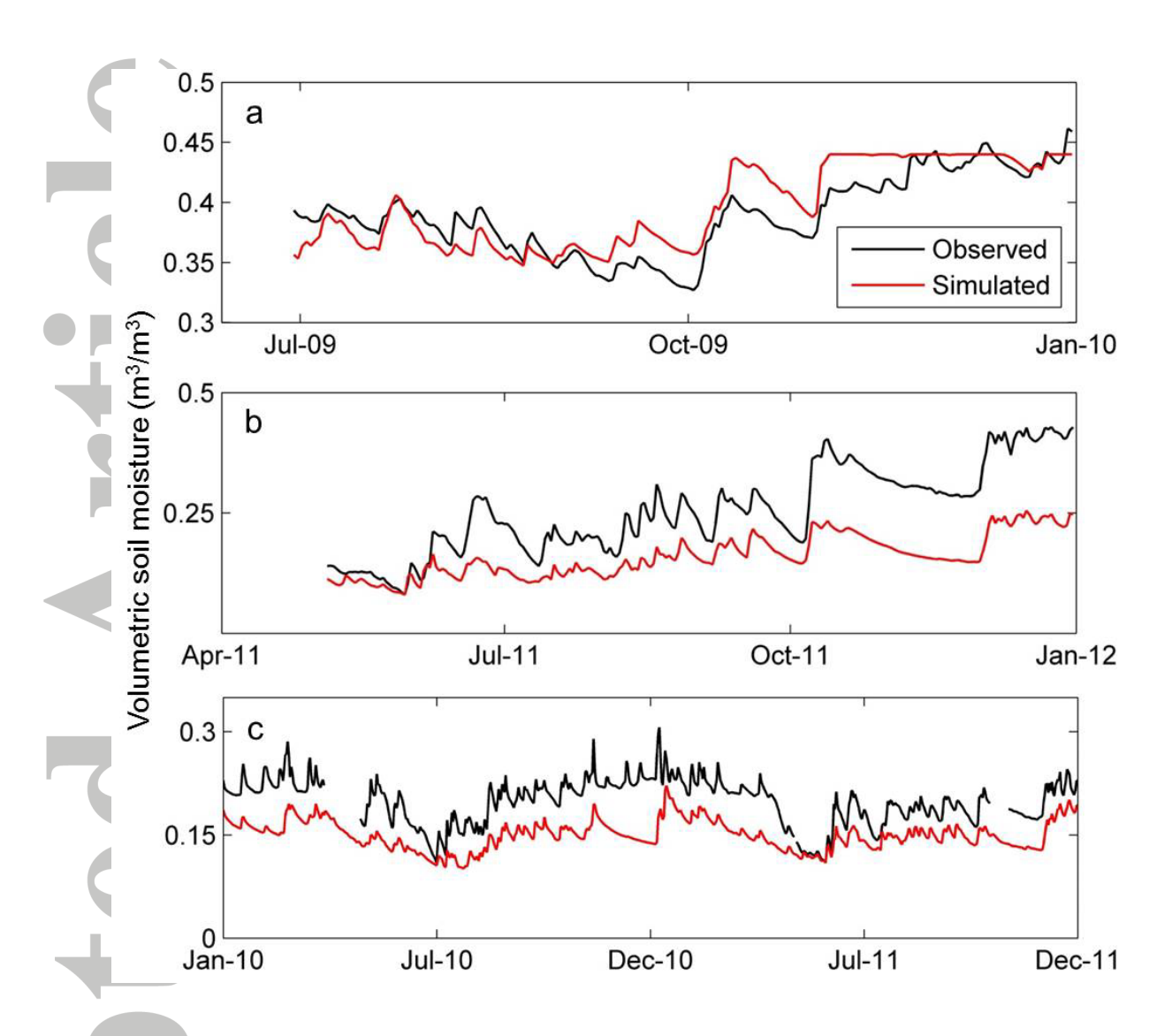


Figure 4. Observed and simulated soil moisture at Wuestebach (a), Rollesbroich (b), and Schoenenseiffen (c) test sites.

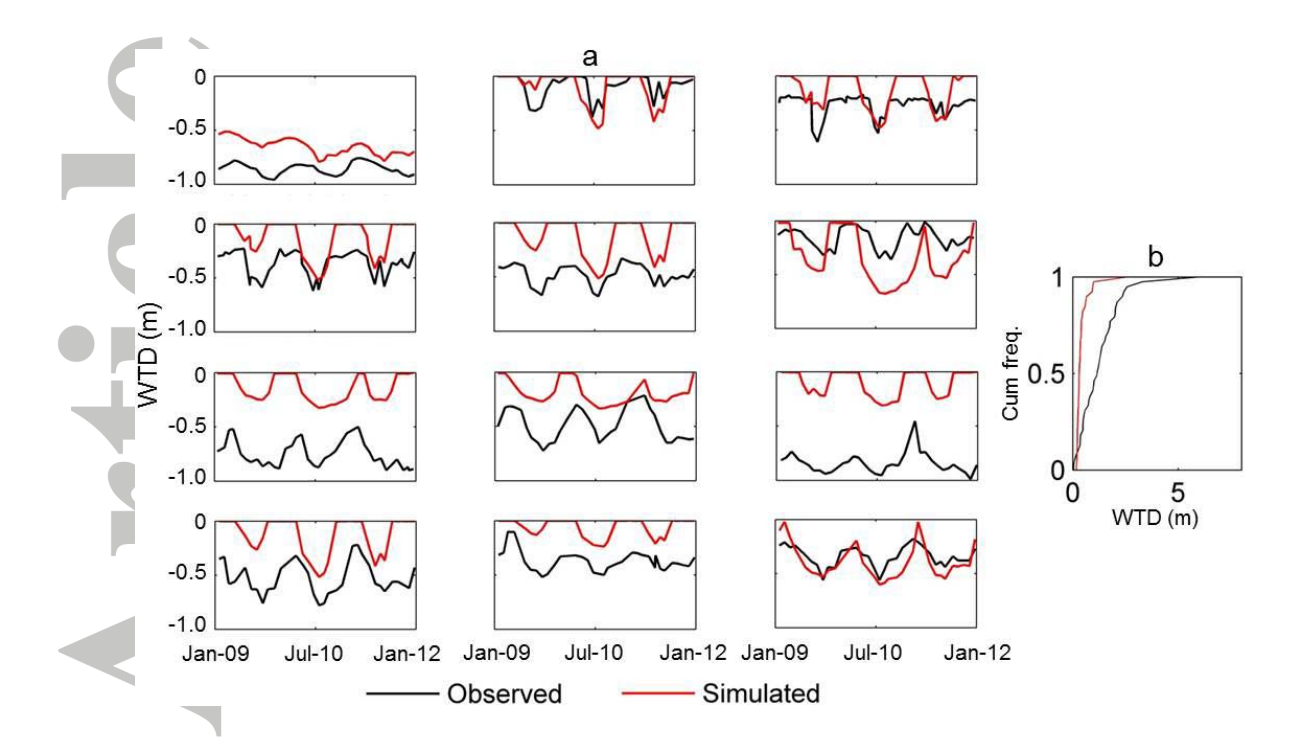


Figure 5. Observed and simulated groundwater table depth, *WTD* time series at 12 selected groundwater wells (a), and cumulative frequency distributions of the observed and simulated *WTD* (b).

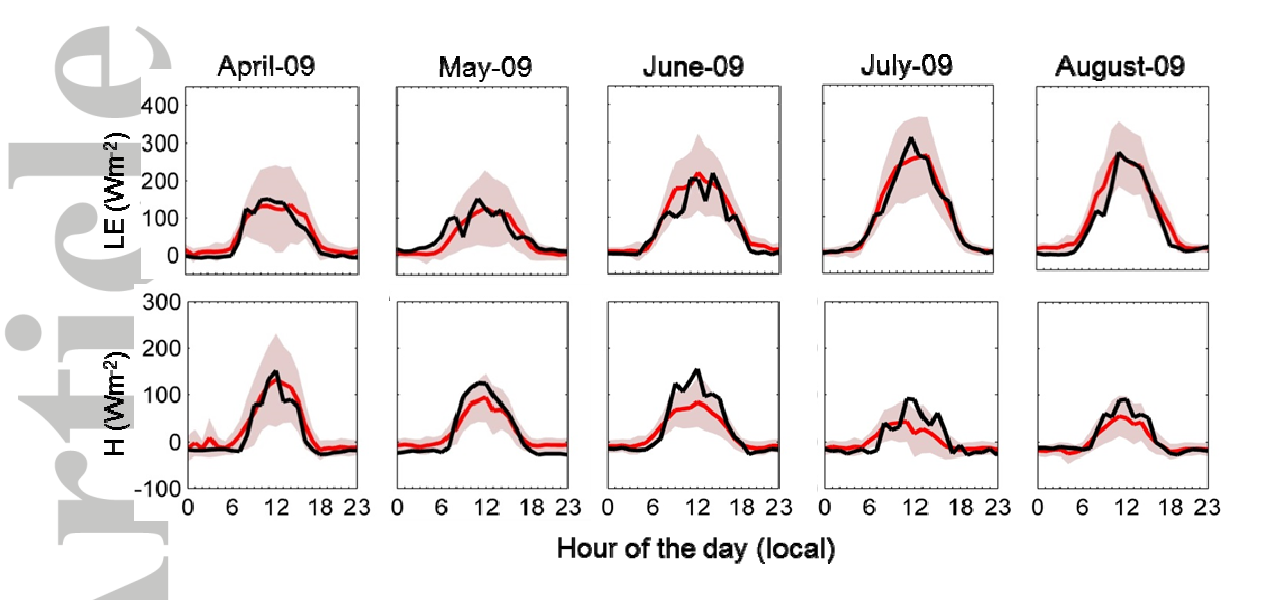


Figure 6. Observed and simulated average daily cycles of latent heat flux, LE, and sensible heat flux, H at the Merken test site. The solid black lines show the mean values of simulated data. The red lines and shaded areas show the mean and standard deviation of observed flux, respectively.

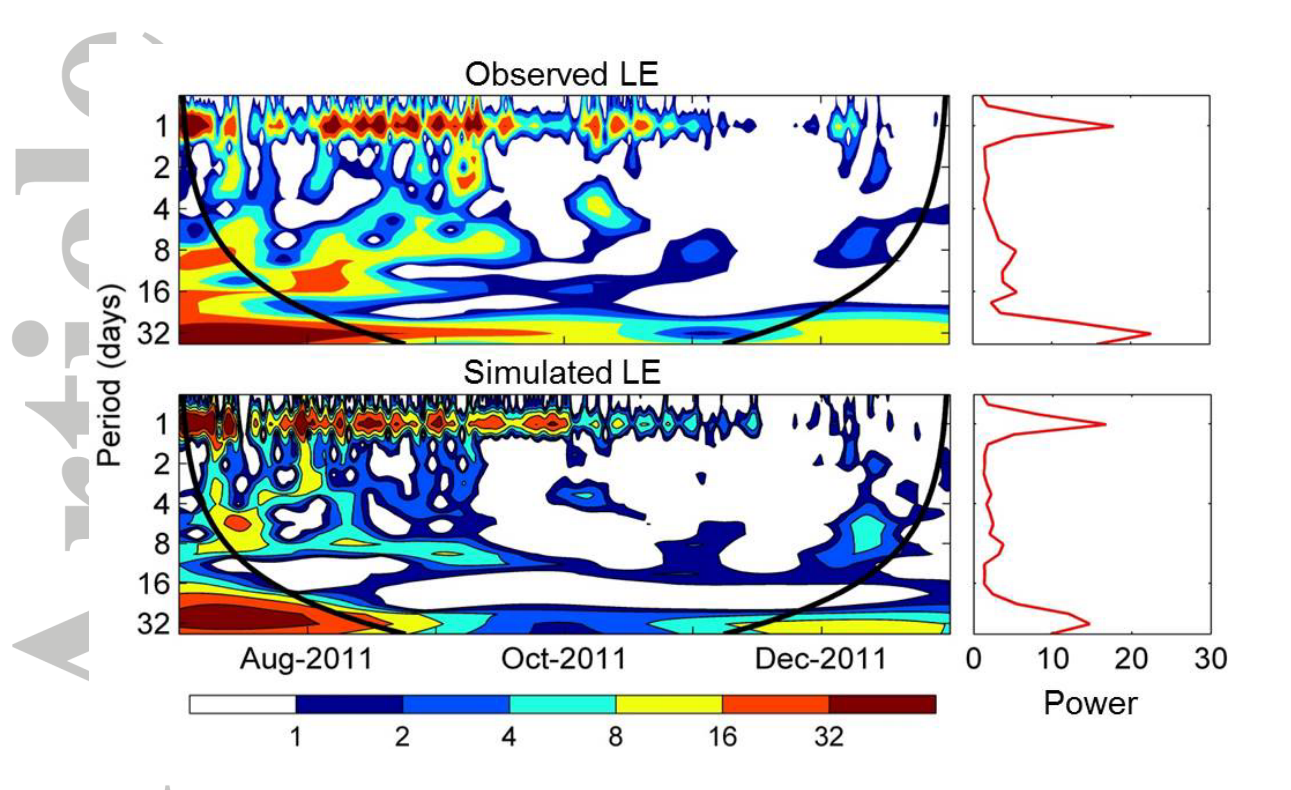


Figure 7. Wavelet transform of observed and simulated latent heat flux, *LE*, at the Merzenhausen test site. The time localized power is shown in the left panels. The cone of influence is indicated with the thick black lines in these plots. The right panels show the global wavelet power.

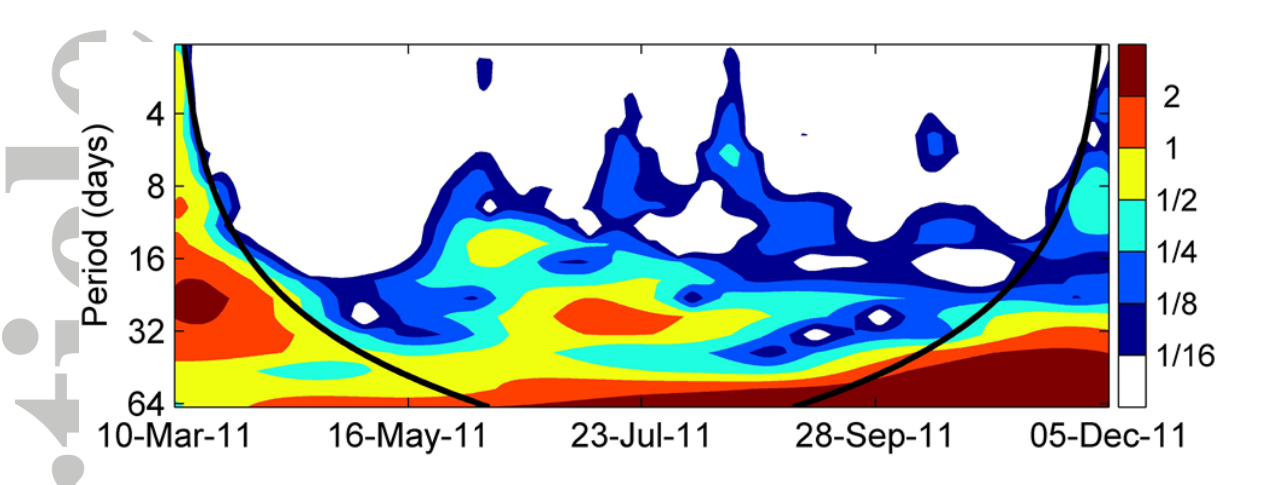


Figure 8. Time localized cross-wavelet power of daily average observed latent heat flux, *LE*, and groundwater table depth, *WTD* time series at the Wuestebach test site.

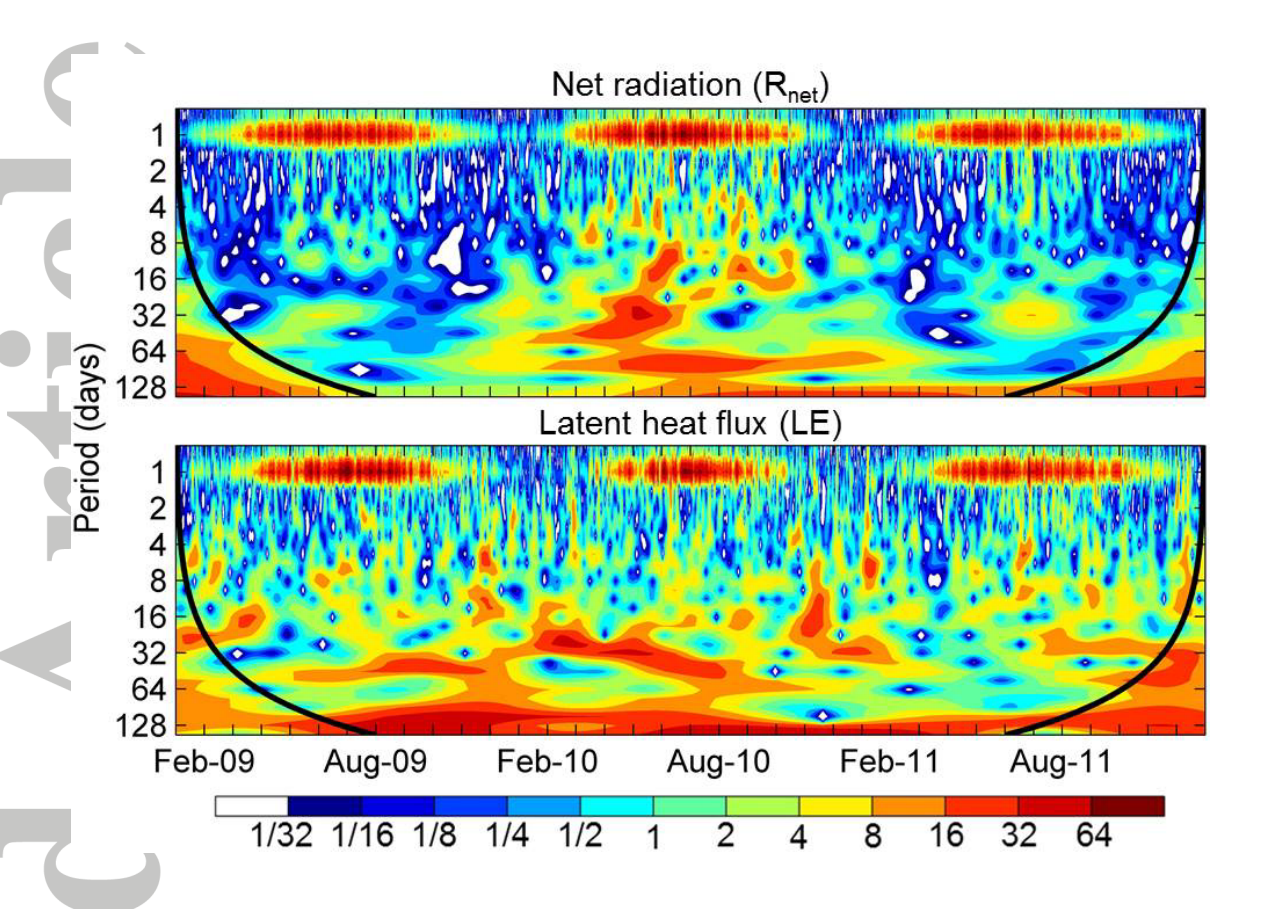


Figure 9. Time localized wavelet power of net radiation, R_{net} , and latent heat flux, LE.

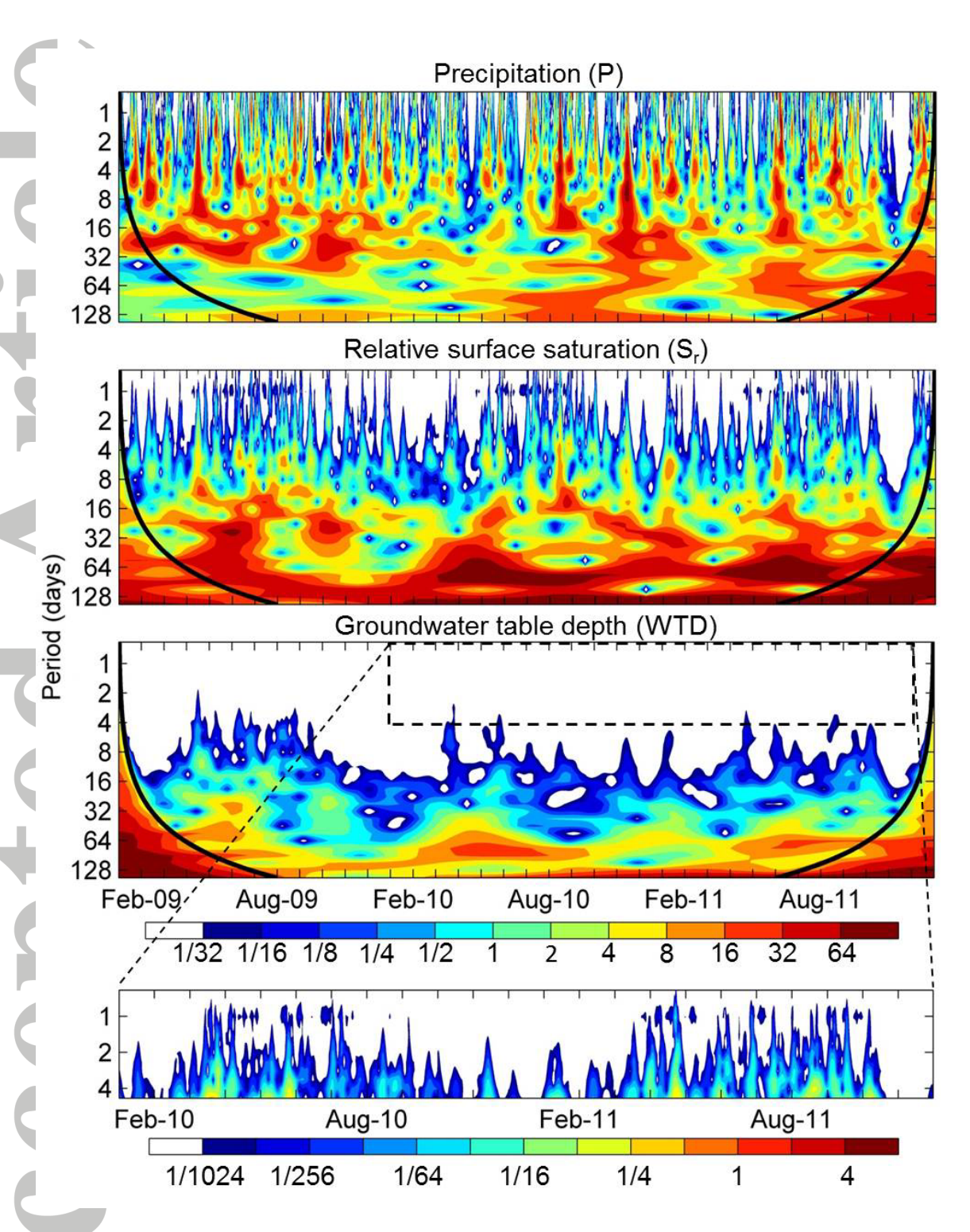


Figure 10. Time localized wavelet power of Precipitation, P, relative surface saturation, S_r , and groundwater table depth WTD. The enlarged part of WTD spectrum (from January 2010 until December 2011) shows the power with small amplitude at 1-4.5day time scale.

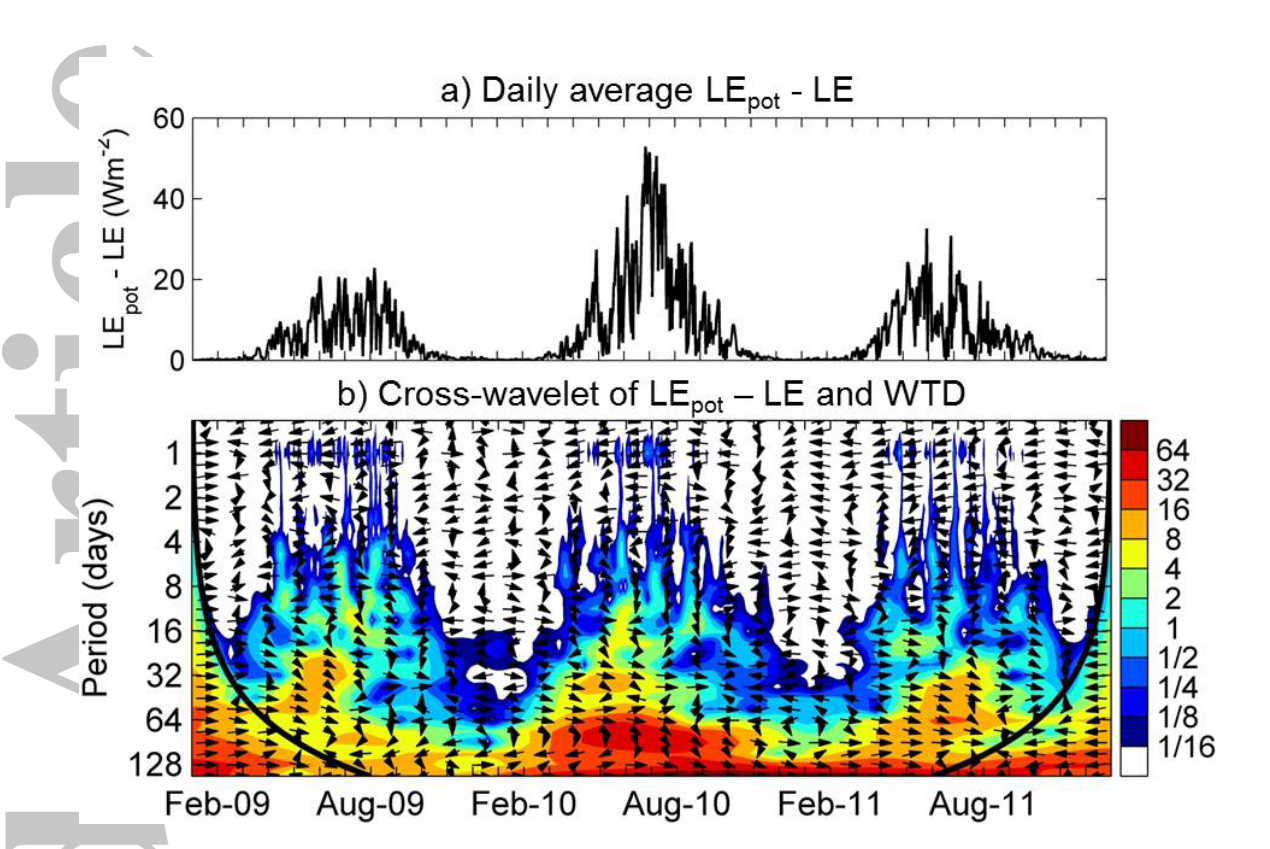


Figure 11. Difference between daily average simulated potential and actual latent heat flux, LE_{pot} - LE (a), and time localized cross-wavelet power of LE_{pot} - LE and water table depth, WTD, over the simulation period. The arrows show the phase relationship between the two time series (right arrow: in phase; left arrow: anti-phase; up arrow: LE_{pot} - LE is leading by 90°; and down arrow: WTD is leading by 90°).

ACC

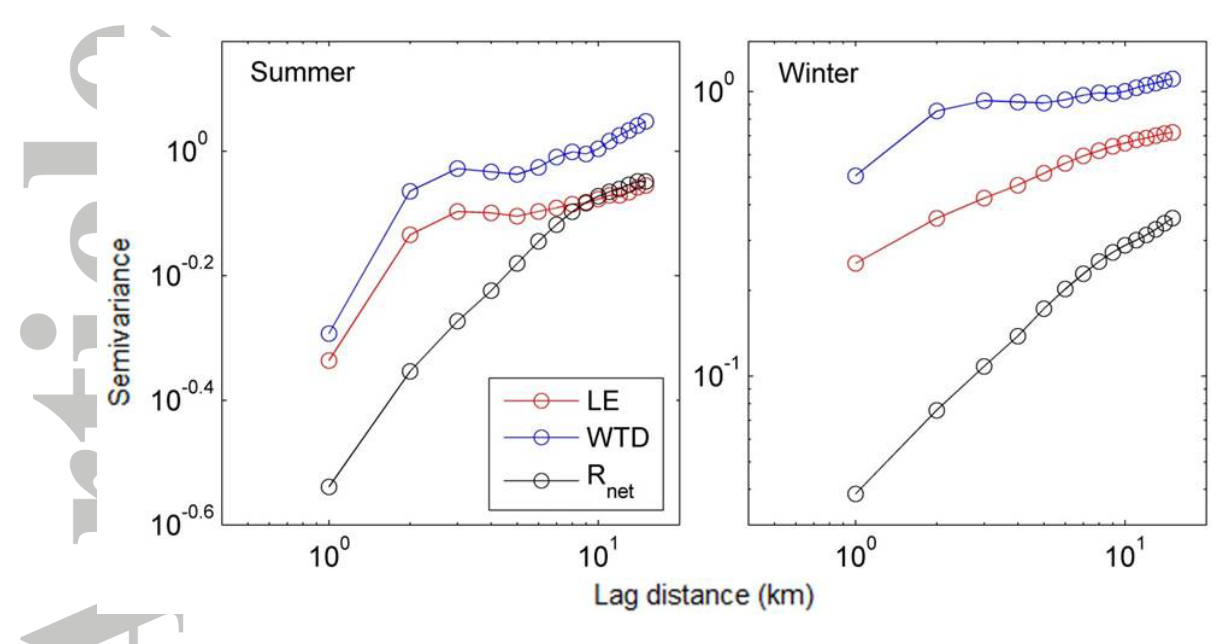


Figure 12. Unit semivariograms of latent heat flux, LE, groundwater table depth, WTD, and net radiation, R_{net} in summer and winter. Note the log-log scale.

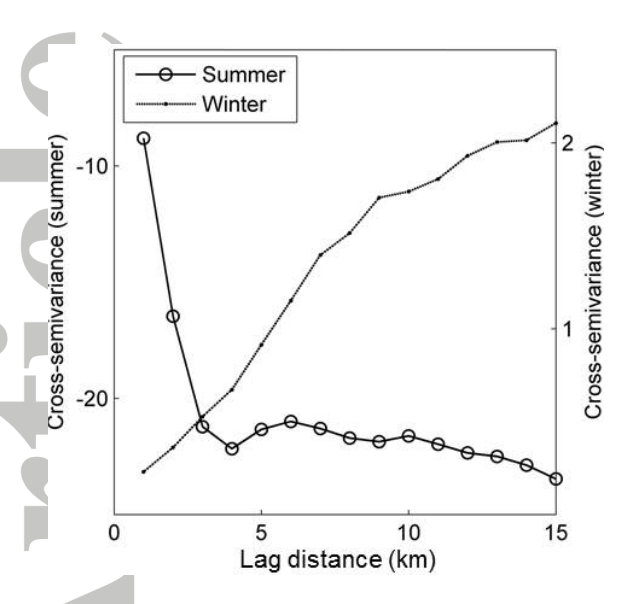


Figure 13. Cross-semivariograms of latent heat flux, *LE*, and groundwater table depth, *WTD* in summer and winter. Note the dual y-axis.